ADVANCED SCIENCE Open Access
www.advancedscience.com

Ubiquitous Order-Disorder Transition in the Mn Antisite Sublattice of the $(MnBi_2Te_4)(Bi_2Te_3)_n$ Magnetic Topological Insulators

Manaswini Sahoo, Ifeanyi John Onuorah, Laura Christina Folkers, Ekaterina Kochetkova, Evgueni V. Chulkov, Mikhail M. Otrokov, Ziya S. Aliev, Imamaddin R. Amiraslanov, Anja U. B. Wolter, Bernd Büchner, Laura Teresa Corredor, Chennan Wang, Zaher Salman, Anna Isaeva, Roberto De Renzi, and Giuseppe Allodi*

Magnetic topological insulators (TIs) herald a wealth of applications in spin-based technologies, relying on the novel quantum phenomena provided by their topological properties. Particularly promising is the $(MnBi_2Te_4)(Bi_2Te_3)_n$ layered family of established intrinsic magnetic TIs that can flexibly realize various magnetic orders and topological states. High tunability of this material platform is enabled by manganese–pnictogen intermixing, whose amounts and distribution patterns are controlled by synthetic conditions. Here, nuclear magnetic resonance and muon spin spectroscopy, sensitive local probe techniques, are employed to scrutinize the impact of the intermixing on the magnetic properties of $(MnBi_2Te_4)(Bi_2Te_3)_n$ and $MnSb_2Te_4$. The measurements not only confirm the opposite alignment between the Mn magnetic moments on native sites and antisites in the ground state of $MnSb_2Te_4$, but for the first time directly show the same alignment in $(MnBi_2Te_4)(Bi_2Te_3)_n$ with $n = 0$, 1 and 2. Moreover, for all compounds, the static magnetic moment of the Mn antisite sublattice is found to disappear well below the intrinsic magnetic transition temperature, leaving a homogeneous magnetic structure undisturbed by the intermixing. The findings provide a microscopic understanding of the crucial role played by Mn–Bi intermixing in $(MnBi_2Te_4)(Bi_2Te_3)_n$ and offer pathways to optimizing the magnetic gap in its surface states.

1. Introduction

The interplay between non-trivial topology and magnetic order has been under the spotlight since the advent of a topological era in condensed matter physics because it may enable versatile and tunable topological phases.[1–5] Magnetic topological materials emerged as an ideal platform for harbouring emergent quantum phenomena of technological relevance, including the quantum anomalous Hall effect (QAHE) and axion electrodynamics.[6–10] A layered (van der Waals) compound $MnBi_2Te_4$, which is a magnetic derivative of the prototypical Bi_2Te_3 topological insulator, has been established as the first intrinsically magnetic TI.[11–14] In this compound, the local moments of the Mn atoms adopt an A-type antiferromagnetic (AFM) order, consisting of a ferromagnetic (FM) alignment within the Mn layer, with AFM stacking in the perpendicular direction.[11,14,15] Combination of a layered crystal structure and the A-type AFM order makes $MnBi_2Te_4$ to fall under the Z_2

M. Sahoo, A. U. B. Wolter, B. Büchner, L. T. Corredor, A. Isaeva
Leibniz IFW Dresden
Helmholtzstraße 20, D-01069 Dresden, Germany
M. Sahoo, L. C. Folkers, E. Kochetkova, B. Büchner
Institut für Festkörper- und Materialphysik
Technische Universität Dresden
01062 Dresden, Germany
M. Sahoo, L. C. Folkers, B. Büchner
Würzburg-Dresden Cluster of Excellence ct.qmat
Dresden, Germany
M. Sahoo, I. J. Onuorah, R. De Renzi, G. Allodi
Dipartimento di Scienze Matematiche
Fisiche e Informatiche
Universitá di Parma
Parco delle Scienze 7A, Parma I-43124, Italy
E-mail: roberto.derenzi@unipr.it
E. Kochetkova, A. Isaeva
Van der Waals-Zeeman Institute
Department of Physics and Astronomy
University of Amsterdam
Science Park 094, Amsterdam 1098 XH, Netherlands
E. V. Chulkov
Donostia International Physics Center
Sebastián 20018 Donostia-San, Spain

The ORCID identification number(s) for the author(s) of this article can be found under https://doi.org/10.1002/advs.202402753

DOI: 10.1002/advs.202402753

topological classification of AFM insulators.[16] The non-trivial value of the invariant, $Z_2 = 1$, stemming from the spin-orbit coupling driven bulk band gap inversion, categorizes it as a 3D AFM TI.[11–14] In the 2D limit, thin $MnBi_2Te_4$ films were theoretically predicted[17,18] and experimentally confirmed to show the AFM axion insulator state,[19,20] as well as the quantized Hall effect, both under external field[19–22] and in remanence.[22]

On top of its exciting intrinsic properties, $MnBi_2Te_4$ also fosters a highly tunable material platform. Multiple tuning knobs, not only extrinsic such as magnetic field, pressure, and temperature, but also intrinsic such as Mn–Mn interlayer distance, variations of the chemical composition, and defect engineering, result in various magnetic and topological states. For example, various pnictogen or chalcogen substitutions and Mn/Bi/Te stoichiometry alternations give rise to such materials as $MnSb_2Te_4$, $MnBi_2Se_4$, or $Mn_2Bi_2Te_5$, whose magnetic and topological properties have been studied both theoretically and experimentally.[23–27] Furthermore, the van der Waals nature of $MnBi_2Te_4$ tolerates interlacing the adjacent ($MnBi_2Te_4$) septuple layers with various number n of nonmagnetic (Bi_2Te_3) quintuple layers, resulting in the $(MnBi_2Te_4)(Bi_2Te_3)_n$ family of stacked structures ($n = 1$ for $MnBi_4Te_7$, $n = 2$ for $MnBi_6Te_{10}$, etc.).[28,29] The increasing distance between the septuple layers progressively weakens the interlayer exchange coupling with an increasing n, which enables an effective tuning of the magnetic structure by moderate magnetic fields,[30–34] or hydrostatic pressure,[35] driving these compounds from the AFM to the FM state. The $(MnBi_2Te_4)(Bi_2Te_3)_n$ materials may host exotic, field-induced topological phases[30,36,37] and temperature-dependent metamagnetic states.[38]

Native defects in these materials are lately in the center of attention thanks to their strong influence on the magnetic and electronic structure.[39–44] They are exploited as an effective tuning knob to purposely modify the latter.[39,45–47] These defects originate from antisite intermixing between the native manganese and pnictogen crystallographic sites. This phenomenon is favored by similar ionic radii, especially those of the Mn and Sb,[48] which enables ca. three times stronger degree of intermixing in $MnSb_2Te_4$ compared to $MnBi_2Te_4$. Specifically, Mn atoms partially occupy the Sb/Bi 6*c* Wyckoff site (Mn_{6c} antisite), while pnictogen atoms swap to the Mn 3*a* site (Bi_{3a} antisite). The amounts of swapped cations do not necessarily fulfill the electroneutrality assumptions for Mn(II) and Sb(III)/Bi(III), and the occurrence of cationic vacancies in both sites is debated.[49] Strong intermixing in $MnSb_2Te_4$ promotes the FM interlayer coupling.[50] The magnetic transition temperature jumps from $T_N = 19$ K in the AFM-like bulk $Mn_{1-x}Sb_{2+x}Te_4$ single crystals[39] to $T_C = 58$ K in the FM-like $Mn_{1+x}Sb_{2-x}Te_4$ ones,[47] which is achieved by varying the growth conditions. (Hereinafter, the main magnetic transition is referred to as T_m, meaning either T_N for AFM or T_C for FM samples.) Moreover, the interlayer coupling can become truly FM in $MnBi_6Te_{10}$ via Mn-Bi defects engineering under appropriate growth conditions.[45,46] This FM coupling may not only help to realize an FM axion insulator state,[36,37] but also the QAHE in contrast to the AFM $MnBi_2Te_4$.[22,51]

Low-temperature neutron diffraction measurements, performed on both the AFM- and FM-like $MnSb_2Te_4$ bulk single crystals, reveal that the local moments of the Mn_{6c} atoms are coupled antiparallel to the Mn_{3a} ones (*ferri*magnetic structure).[39,52] However, for the $(MnBi_2Te_4)(Bi_2Te_3)_n$ family the magnetic role of the antisites has not been decisively established yet. Indeed, the available neutron diffraction data[53–55] do not shed light on this issue (likely because of the much lower levels of intermixing as compared to $MnSb_2Te_4$), although the high-field magnetization studies performed on $MnBi_2Te_4$ do suggest that there is an AFM coupling between the Mn_{6c} and Mn_{3a} sublattices.[40]

To close this important gap, this article systematically investigates the magnetic behavior of the antisites in polycrystalline $(MnBi_2Te_4)(Bi_2Te_3)_n$ with $n = 0$, 1, 2 and in one $MnSb_2Te_4$ sample by means of local magnetic probes, namely nuclear magnetic resonance (NMR) (Section 2) and muon spin spectroscopy (μSR) (Section 3). Both techniques probe the dynamic and thermodynamic material properties, as well as the disorder introduced by the antisites. The measurements are performed in applied and in zero (ZF) external magnetic field, and ^{55}Mn NMR provides direct local evidence of the nearly opposite relative spin alignment of Mn_{3a} and Mn_{6c} for all compounds studied here. Importantly, NMR reveals a magnetic order-disorder transition in the Mn_{6c} sublattice of $MnSb_2Te_4$ well below $T_m = 27$ K. This clearly discriminates two regions in the $MnSb_2Te_4$ magnetic phase diagram: i) $T < T^* < T_m$, when the Mn_{6c} and Mn_{3a} moments are coupled antiferromagnetically; and ii) $T^* < T < T_m$, when the Mn_{6c} sublattice is paramagnetic-like, whereas the Mn_{3a} one sustains its intra- and interlayer orders. μSR and bulk magnetometry measurements confirm the same order-disorder transition in the Mn_{6c} sublattice of all studied $(MnBi_2Te_4)(Bi_2Te_3)_n$ as well.

E. V. Chulkov
Departamento de Polímeros y Materiales Avanzados: Física, Química y Tecnología, Facultad de Ciencias Químicas
Universidad del País Vasco UPV/EHU
Donostia-San Sebastián 20018, Spain

E. V. Chulkov
Centro de Física de Materiales (CFM-MPC)
Centro Mixto (CSIC-UPV/EHU)
Donostia-San Sebastián 20018, Spain

E. V. Chulkov
Saint Petersburg State University
Saint Petersburg 199034, Russia

M. M. Otrokov
Instituto de Nanociencia y Materiales de Aragón (INMA)
CSIC-Universidad de Zaragoza
Zaragoza 50009, Spain

Z. S. Aliev, I. R. Amiraslanov
Baku State University
Baku AZ1148, Azerbaijan

Z. S. Aliev, I. R. Amiraslanov
Institute of Physics Ministry of Science and Education Republic of Azerbaijan
Baku AZ1143, Azerbaijan

C. Wang, Z. Salman
Laboratory for Muon Spin Spectroscopy
Paul-Scherrer-Institute
Villigen PSI CH-5232, Switzerland

A. Isaeva
Faculty of Physics
Technical University of Dortmund
Otto-Hahn-Str. 4, 44221 Dortmund, Germany

A. Isaeva
Research Center Future Energy Materials and Systems (RC FEMS)
Germany

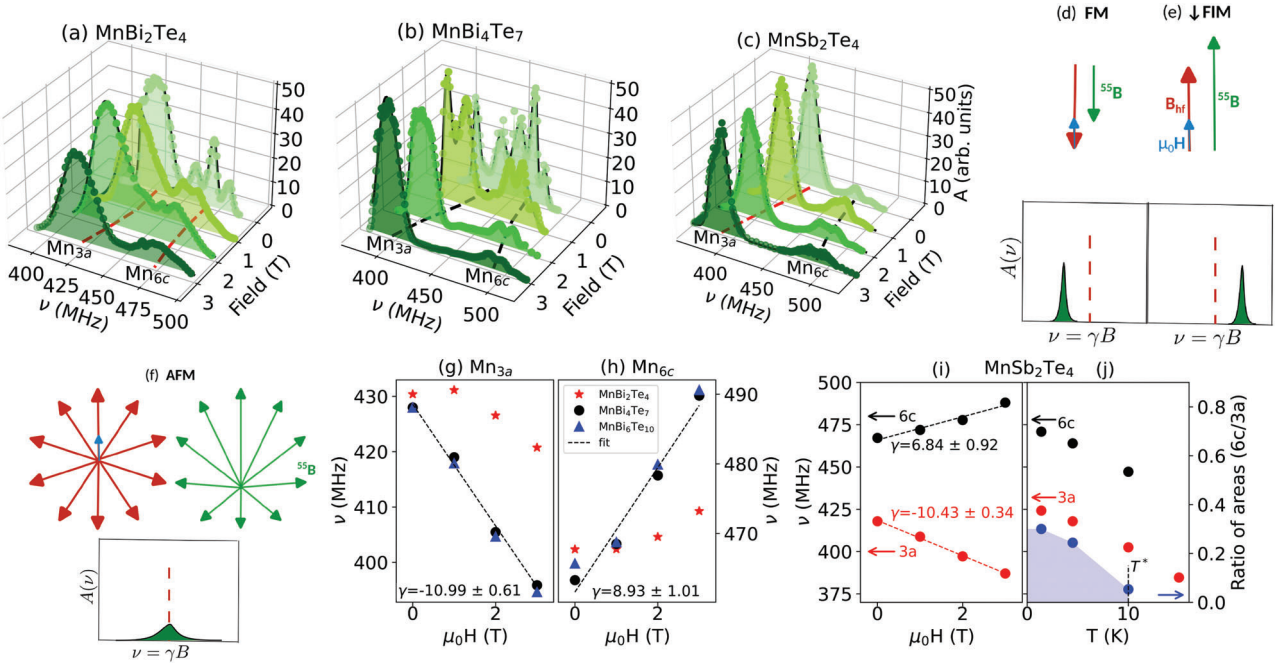

Figure 1. a–c), ^{55}Mn NMR spectra of $MnBi_2Te_4$ (α sample), $MnBi_4Te_7$ and $MnSb_2Te_4$ respectively, at T = 1.4 K in increasing applied fields, starting from ZF; d–f) polycrystal vector composition $^{55}\mathbf{B} = \mu_0\mathbf{H} + \mathbf{B}_{hf}$ and their resulting spectral shifts for three simple cases: soft ferromagnet (FM, d), soft ferrimagnet, minority spin (↓FIM, e), antiferromagnet (AFM, f); g,h) field dependence of the Mn_{3a} and Mn_{6c} mean frequency peaks for the $(MnBi_2Te_4)(Bi_2Te_3)_n$ family; i,j) Mn_{3a} and Mn_{6c} peaks for $MnSb_2Te_4$, field dependence (i) and temperature dependence (j) of their frequencies (black, red dots), temperature dependence of the ratio of their areas (blue dots, j).

The discovery of the loss of the Mn_{6c} sublattice magnetic ordering is highly relevant in the context of the crucial role that Mn-Bi intermixing plays in the reduction of the gap at the Dirac point in $MnBi_2Te_4$.[41–44,56–61]

2. The Antisites From the NMR Perspective

In this and the next section, we describe a unified picture emerging from NMR and μSR, skipping the technical details of its derivation for the sake of clarity. The principles of the two techniques are briefly described in Section 5 and further important details are provided in the Supporting Information.[62] Section 5 and the Supporting Information also give details about the sample preparation and characterization; the protocols are based on our previous works,[28–30,45,48,63] which ensures consistency between all our published series of samples in terms of structural and magnetic properties.

In ZF-NMR, ^{55}Mn nuclear spins (gyromagnetic ratio $^{55}\gamma$ = 10.576 MHz/T) precess around a very large hyperfine field B_{hf}, between 40 and 45 T at 1.4 K. B_{hf} is primarily due to the negative coupling, $-\mathcal{A}$, to the on-site moment $g\mu_B\mathbf{S}$, with much smaller positive couplings $\mathcal{B}$ to six nearest neighbors Mn_{3a}, and even smaller distant dipole contributions, so that in first approximation, assuming parallel $\mathbf{S}$ in the layer, the NMR frequency is $^{55}\nu = {}^{55}\gamma(\mathcal{A} - 6\mathcal{B})g\mu_B\mathbf{S}$.

2.1. NMR Peak Assignment

A 3D view of the spectra for polycrystalline samples of $MnBi_2Te_4$, $MnBi_4Te_7$ and $MnSb_2Te_4$ at T = 1.4 K, in the frequency range 350 to 500 MHz, is shown in **Figure** 1a–c ($MnBi_6Te_{10}$ in the Figure S8, Supporting Information[62]) with ZF at the back and increasing fields $\mu_0 H$ towards the front. They all show two broad peaks patterns, each centered at a distinct frequency: $\nu_{a,c} = {}^{55}\gamma\,|{}^{55}\mathbf{B}_{a,c}|$. Therefore two distinct Mn sites experience a different total local field modulus $^{55}B_{a,c}$, i.e., different values of B_{hf}, as it would be expected for the main site Mn_{3a} and the anti-site Mn_{6c}. The 5–10% breadth of the frequency peaks is due to disorder in their vicinity, producing small variations of the local electronic environment, reflected in B_{hf}.

The relative area under the two peaks at 3T assigns the lower-frequency, majority peak to Mn_{3a} and the minority peak to Mn_{6c} (Figure 1a–c, the proportionality of the signal amplitude with the number of nuclei may not be guaranteed in ZF but it is recovered in 3T, see Section NMR). The frequencies confirm the assignment, since the six non-negligible transferred couplings $\mathcal{B}$ of Mn_{3a} and the three nearly vanishing ones for Mn_{6c} are both opposite to the on-site coupling $\mathcal{A}$. This simple argument is confirmed by DFT simulations of the hyperfine coupling at the Mn sites (Figure S9, Supporting Information).

2.2. Antisite Spin Alignment

The same 3D plots (Figure 1a–c) show that the frequency splitting increases with the applied field. This can be understood from the field vector composition $^{55}\mathbf{B} = \mu_0\mathbf{H} + \mathbf{B}_{hf}$. In simple cases, the relative local orientation of the Mn_{3a} and Mn_{6c} magnetic moments is easily inferred from this vector composition, as shown in Figure 1d–f

$$^{55}\nu(H) = \nu_{hf}\begin{cases} -\,^{55}\gamma\,\mu_0 H & \text{FM, } \uparrow \text{ FIM} \\ +\,^{55}\gamma\,\mu_0 H & \downarrow \text{ FIM} \\ +\,\mathcal{O}\left(\left[\frac{\mu_0 H}{B_{hf}}\right]^2\right) & \text{AFM} \end{cases} \quad (1)$$

Namely, in the FM case, or equivalently, for the large magnetization sublattice of a ferrimagnet (↑ FIM) the moments align along the applied field, hence $\mathbf{B}_{hf}$ is opposite to $\mathbf{H}$ and the frequency decreases with increasing field. On the other hand, they anti-align to $\mathbf{H}$ for the small magnetization sublattice of a ferrimagnet (↓ FIM), so there the frequency grows with $\mathbf{B}_{hf}\|\mathbf{H}$. Finally, in the collinear AFM case, they do not align, and the superposition of all relative vector orientations in our polycrystalline samples leads to a broadening with no first order shift.[62]

Figure 1g,h shows the shifts vs. applied field for the $(MnBi_2Te_4)(Bi_2Te_3)_n$ samples. The majority Mn_{3a} peak of $MnBi_2Te_4$ (red stars) does not shift with H up to 1 T, following the AFM behavior predicted by Equation (1). Its small shift for 2 T$\lesssim H \leqslant$ 3 T is consistent[62] with a canted antiferromagnetic (CAFM) state.[64–66] In contrast, $MnBi_4Te_7$ and $MnBi_6Te_{10}$ (black and blue symbols, respectively) follow the FM case, like the $MnSb_2Te_4$ majority site, shown by the red symbols in Figure 1i, all fitted with negative slopes equal to $\gamma = -^{55}\gamma$ within error bars.

Neutron diffraction measurements on $MnSb_2Te_4$ have revealed the antiparallel alignment of the Mn_{3a} and Mn_{6c} local moments.[39,52] In our NMR data, this spin alignment is directly demonstrated in Figure 1i by the positive slope of $^{55}\nu(H)$ for the Mn_{6c} sites. Moreover, we see exactly the same behavior for all $(MnBi_2Te_4)(Bi_2Te_3)_n$ materials (Figure 1g,h), i.e., their septuple layers show the same FIM structure as $MnSb_2Te_4$. While indications of this behavior in $MnBi_2Te_4$ were previously seen in high-field magnetometry,[40] the presented NMR results provide direct local evidence of the opposite spin alignment of Mn_{3a} and Mn_{6c} for *all* $(MnBi_2Te_4)(Bi_2Te_3)_n$ with $n = 0$, 1 and 2. It is likely that the $n > 2$ members of the $(MnBi_2Te_4)(Bi_2Te_3)_n$ family[37,67,68] should also display this FIM structure, pretty much as their $n = 0 - 2$ analogs. Note that the $^{55}\nu(H)$ slope for $(MnBi_2Te_4)(Bi_2Te_3)_n$ in Figure 1h is slightly reduced[62] by an average canting angle θ between the sublattice magnetization and $\mathbf{H}$, according to $\gamma = {}^{55}\gamma\cos\theta$. This angle is small for the FM-like materials, but quite sizable for CAFM $MnBi_2Te_4$, reflecting the large powder average angle between the magnetization of its canted Mn_{3a} sublattices and the field.

2.3. Antisite Moment Temperature Dependence

The ^{55}Mn NMR signal quickly disappears when increasing the temperature above T = 1.4 K, as the NMR T_2 relaxation time gets shorter than the instrumental dead-time. For $MnSb_2Te_4$ the Mn_{3a} ZF NMR frequency (red symbols in Figure 1j) is detected up to $t = T/T_m \approx 0.6$, whereas the Mn_{6c} ZF NMR frequency (black symbols) is detected only up to $t = 0.4$. They both decrease toward the second order transition at T_m, following the order parameter. However, the ratio of their peak areas (blue symbol) decreases much more quickly over the same range, vanishing around t = 0.4. This implies that the Mn_{6c} peak disappears in a first-order-like fashion at a temperature T^* well below T_m.

Summarizing, NMR at 1.4 K directly detects the opposite alignment of the Mn_{3a} and Mn_{6c} sublattices in all of the systems studied here, and it demonstrates that in the Sb-based compound the antisite Mn_{6c} disorders above T^*, well below T_m. The same information is not accessible for $(MnBi_2Te_4)(Bi_2Te_3)_n$, due to a combination of lower ordering temperatures and shorter T_2.

3. μSR Results

Spin-polarized muons implanted in polycrystalline samples stop in few lowest energy interstitials. In ZF and for $T < T_m$ the muon spin precesses around the local magnetic field B_μ, due to ordered moments, producing coherent oscillations at a frequency $\gamma_\mu B_\mu$ in the asymmetry of the muon decay at early times (γ_μ = 135.554 MHz/T, see Section 5).

Selected ZF-μSR early-time asymmetries $A(t)$ are shown in **Figure 2a–c** for the $(MnBi_2Te_4)(Bi_2Te_3)_n$ materials at different temperatures, with their best fit to a minimal model, Equation (2) in Section 5. The model describes the internal field distribution $p(B_\mu)$ probed by muons as a few Gaussian components of very broad width ΔB_i. Starting from $MnBi_2Te_4$ (Figure 2a), the asymmetry shows a fast, over damped initial relaxation and a second damped oscillation below T_m. Both components correspond to appreciable internal fields, the fast initial Gaussian decay to a mean value smaller than its width $0 \lesssim B_1 < \Delta B_1$, and the visible oscillation to an observable mean value $B_2 > \Delta B_2$. At low temperature a third oscillating component ($B_3 > \Delta B_3$) appears. By comparison, the $n = 1$, 2 members differ from $n = 0$ in *i)* the absence of the $B_1 < \Delta B_1$ fast initial decay and *ii)* a lower field B_2 value, whereas, they also display *iii)* a high field B_3 component, that sets in only at lower temperatures. The presence of two distinct oscillations, both heavily damped, is more evident in the low temperature best fits of Figure S10 (Supporting Information).[62]

3.1. Magnetic Transitions

The temperature dependence of the internal fields, $\Delta B_1(T)$ (the width of that distribution), $B_2(T)$ and $B_3(T)$, are shown in Figure 2d–f. It reveals two common features among all three family members: ΔB_1 and B_2 correspond to the order parameter and vanish at the second-order magnetic transitions, T_m; in contrast, B_3 vanishes abruptly at T^*, inside the ordered phase, without any corresponding anomaly in ΔB_1, B_2.

Weak transverse field (WTF) μSR provides the amplitude of the spin precession in a small applied field ($\mu_0 H \ll \Delta B_1$, B_2, B_3). Below T_m this amplitude drops abruptly. The $(MnBi_2Te_4)(Bi_2Te_3)_n$ *magnetic volume fraction* m_{wtf} shown in Figure 2g–i is obtained from WTF measurements (Equation (4) in Section 5) and demonstrates that $MnBi_2Te_4$ and $MnBi_6Te_{10}$ undergo very sharp transitions, at T_m, (the width of the transition for a 90%–10% volume reduction is $\Delta T < 1$ K), despite their relatively large atomic disorder implied by the presence of antisites. The $n = 1$ sample displays a sharp transition as well, but a 20% contribution, which we attribute to intergrowths of the $MnBi_2Te_4$ phase, is also visible (Figure 2h).

Similar results were obtained for $MnSb_2Te_4$.[69] Notably, we measured two distinct $MnBi_2Te_4$ samples, labeled α and β (filled

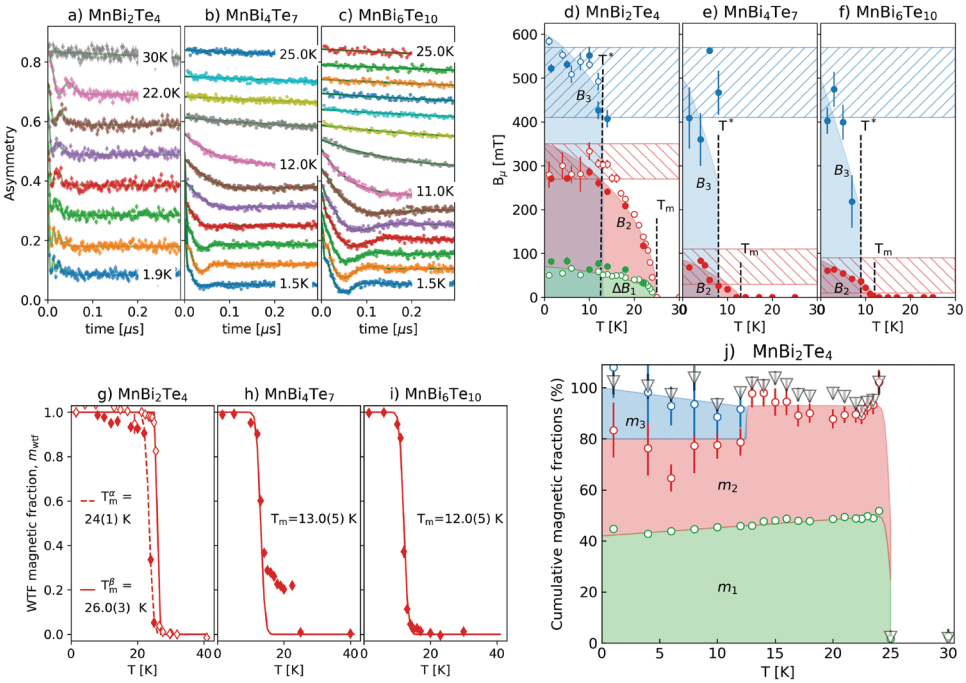

Figure 2. μSR in $(MnBi_2Te_4)(Bi_2Te_3)_n$, $n = 0, 1, 2$. a–c) Early time ZF asymmetries at various temperatures with best fits (solid curve), displaced vertically for clarity; d–f) Temperature dependence of the internal fields ΔB_1, B_2, B_3 (green, red, blue symbols, respectively), the hatched bands show the values predicted by DFT at $T = 0$, shaded areas are guides to the eye (Equation (7)); g–i) WTF magnetic volume fraction m_{wtf} versus temperature; j) ZF transverse cumulative magnetic fractions m_1 (green circles), $m_1 + m_2$ (red circles) and $m_1 + m_2 + m_3$ (blue circles), plus longitudinal magnetic fraction m_L (grey triangles), cfr. Equation (2). Data in panel (a) and open symbols in panel (d,g,j) correspond to the $MnBi_2Te_4$ β sample.

and open symbols, respectively, in Figure 2d,g,j), which readily show distinguishable transitions (T_m = 26.0(3), 24(1) K), due to slightly different preparation conditions. The residual WTF amplitude well below T_m is due to a small fraction of muons implanted outside the sample, that do not experience its spontaneous internal magnetic field distribution.

Separate magnetic volume fractions m_i are also derived from the ZF normalized amplitudes at each internal field B_i (Equation (5), Section μSR). Independently, the total volume fraction m_L is obtained from the longitudinal amplitude (Equation (6)). Figure 2j shows the cumulative sum of the three transverse fractions for $MnBi_2Te_4$-β. Both m_L (grey symbols) and m_1 + m_2 (red symbols) drop sharply at the transition T_m, in agreement with m_{wtf}. In contrast, m_3 disappears abruptly at T^* = 12(1) K, suggesting that this component originates from muon sites sensitive to the subtle change that takes place across that point. This is reminiscent of our NMR $MnSb_2Te_4$ results. For the $(MnBi_2Te_4)(Bi_2Te_3)_n$ samples, the temperature coincides with a clear anomaly appearing in magnetization (Figure S7 and Table SI, Supporting Information), suggesting that Mn_{6c} moment are undergoing fast (paramagnetic-like) reorientations above T^*. Further insight crucially requires the correct identification of the muon-stopping sites.

3.2. The Antisites from the μSR Perspective

The muon sites were identified and their respective $T = 0$ K field values, B_μ, were computed using a standard protocol, known as DFT+μ,.[70–73] These are explained briefly in Section 5 and discussed in more details in the Supporting Information.[62] In the ideal $MnBi_2Te_4$ crystal, this protocol identifies three stable sites, shown in **Figure 3** as Te-μ-Mn (red sphere), Te-μ-Bi (blue sphere), and Te-μ-Te (yellow sphere) and reported in the top box of **Table 1**. The mean field values at these sites agree nicely with the experimental component B_1 (Te-μ-Bi and Te-μ-Te) and B_2 (Te-μ-Mn), respectively. Notice that the correspondence between sites and fields is not bijective (more sites may contribute to the same field distribution) and that the uncertainty in the DFT+μ derived values is below 25%.

The presence of intermixing modifies these findings in two ways: i) inherent disorder broadens considerably all field distributions, producing large widths ΔB_i, and ii) the extra moment modifies significantly the mean field values at muon sites nearest neighbor (nn) to Mn_{6c} and Bi_{3a}. We label these two modified sites as Te-μ-Mn@Bi and Te-μ-Bi@Mn, respectively, and report their properties in the lower box of Table 1. Both these consequences are observed experimentally, in particular the calculation for the muon site Te-μ-Mn@Bi agrees with local field B_3, while Te-μ-Bi@Mn contributes to B_1.

Let us now turn to the $(MnBi_2Te_4)(Bi_2Te_3)_n$ compounds with $n = 1, 2$, where the sites closest to the Mn_{3a} layer are predicted to be very similar to those of $n = 0$. The farther high symmetry Te-μ-Te site, instead, is replaced by more than one site in the intervening quintuple layers. Since all of them are far removed from Mn_{3a}, we expect a large majority of muon sites characterized by very small or vanishing local field values. However, n = 1, 2 samples show non-vanishing net magnetic moment, hence

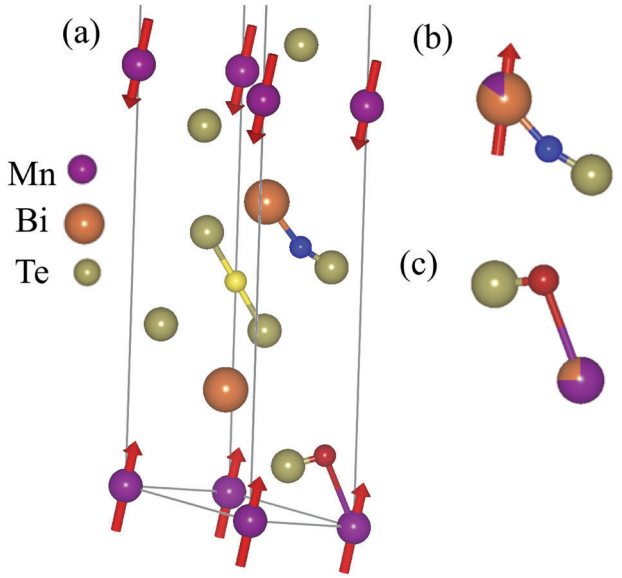

Figure 3. Representative muon sites as small colored atoms in $MnBi_2Te_4$ (and $MnSb_2Te_4$) by DFT+μ: Te-μ-Mn (red), Te-μ-Bi (blue atom), Te-μ-Te (yellow). a) Half the primitive cell with Mn_{3a} only, b) Te-μ-Mn@Bi and c) Te-μ-Bi@Mn.

B_μ has an additional Lorentz field term $B_L = 4\pi M/3 \approx 70$, 50 mT, respectively. This contributes negligibly to the high field of the Te-μ-Mn@Bi site, $B_3 \gg B_L$, but significantly to the low field Te-μ-Bi@Mn, Te-μ-Bi and Te-μ-Te sites. This justifies both the second experimental field value $B_2 \approx B_L$ (Figure 2e,f), its large fraction f_2 and the disappearance of the f_1, $B_1 = 0$ signal.

The agreement of all these predictions, shown as hatched color bands in Figure 2d–f, with $T \to 0$ K experimental data is altogether remarkable. It is the more so, in as much the same three DFT muon sites support a coherent, simple interpretation of the data for up to three experimental fit components, in four different compounds, over two magnetic phases.

4. Discussion and Conclusion

An important result from NMR is that the size of the moment on Mn obtained from the hyperfine field, in first approximation, is proportional to the on-site coupling $\mathcal{A}$, which is roughly 10 T/μ_B for all 3d ions and for ^{55}Mn in particular.[74–76] An estimate of this coupling comes from the ZF NMR frequency of Mn_{3a} and Mn_{6c}. Taking the value of the latter for its much smaller transferred terms $\mathcal{B}$, and, conservatively, half their difference as the uncertainty, we get roughly the same moment for all three $(MnBi_2Te_4)(Bi_2Te_3)_n$ samples, $\mu_{Mn} = 4.3(2)\,\mu_B$, in agreement with neutron diffraction.[77]

Importantly, fast Mn_{6c} spin fluctuations above T^* justify the disappearance of the f_3 component, assigned consistently to the Te-μ-Mn@Bi site and mostly due to the nn Mn_{6c} moment. This observation is common to all three compositions. We recall that the same conclusion is drawn from the NMR findings on $MnSb_2Te_4$ (Section 2), confirmed by μSR as well.[62] In addition, μSR results confirm the first order character of T^*, since the internal field B_3, proportional to the Mn_{6c} moment, is still large when the signal amplitude vanishes (Figure 2d–f, mimicking the NMR results of Figure 1j).

The anomaly at T^* is confirmed by magnetization data,[62] which, however, are obtained in an applied field. Recall that in $MnBi_6Te_{10}$ the local field B_2 is assigned to the low field sites Te-μ-Bi, Te-μ-Te, and Te-μ-Bi@Mn,[62] in the presence of an additional comparable Lorentz field, B_L, due to the net domain magnetization. The smooth behavior of B_2 across T^* indicates that B_L survives also in zero applied field above the transition, suggesting that a dominant FM stacking of Mn_{3a} layers persists above T^* in zero field, therefore it is not induced by the external field.

The orientation of the antisite static moments successfully shows the sign of their dominant local exchange, displaying a universal behavior in this family, but this does not tell us the full magnetic structure of each material, that varies in the family. Actually, for $MnBi_2Te_4$ we can assume that T_m is a Néel transition and the sample is AFM in zero field. Here, T^* (detected in ZF) clearly merges with the low temperature transition seen in $M(T)$ (Figure S1, Supporting Information[62]). For $MnBi_4Te_7$ the presence of a cusp in $M(T)$ suggests AFM bulk behavior at T_m, but μSR shows the presence of an $n = 0$ contribution and we avoid further considerations. Finally, $MnBi_6Te_{10}$ was already shown to be FM under certain growth conditions,[29,45,46] which we reproduce in this work as well.

Figure 4 summarizes our findings in a schematic phase diagram for the A-type antiferromagnet $MnBi_2Te_4$, where the $T \to 0$ magnitude of the static Mn moment is taken from NMR and its temperature behavior from the interpolation by Equation (7) on the ZF μSR fields $\Delta B_1(T)$, $B_2(T)$, of Figure 2d. The blue region is characterized by the static ordering of the diluted Mn_{6c} moments, aligned antiparallel to the main Mn_{3a} moments, as NMR demonstrates. The static moment at Mn_{6c} vanishes in the red region.

A similar plot for $MnBi_6Te_{10}$ is reported in the Supporting Information[62] ($MnBi_4Te_7$ data are less reliable due to the presence of a sizable fraction of $MnBi_2Te_4$ layer intergrowths, Figure 2h; Figure S4, Supporting Information). Remarkably, in all three compositions, the mean Mn_{3a} order does not change appreciably across T^*.

The red-shaded high-temperature phase is characterized by a very sharp second-order transition, as it is witnessed in all samples by the abrupt vanishing of the magnetic volume fraction, both by WTF and ZF μSR (Figure 2g–i). We highlight the unique ability of μSR, as opposed to both magnetometry and neutron

Table 1. $T = 0$ local field at the representative muon sites in $MnBi_2Te_4$, identified by color as in Figure 3 (see Supporting Information for details.[62]) Filled circles refer to muon sites: first three rows, far from antisites; last two rows, nn to an antisite. Colored dashes refer to colors of symbols in Figure 2d.

Muon site label	nn antisite	DFT+μ B_μ(mT)	Experiment	
			B_i (mT)	term
● Te-μ-Bi	–	93	0(80)	$-\Delta B_1$
● Te-μ-Te	–	0		
● Te-μ-Mn	–	314	290(10)	$-B_2$
● Te-μ-Mn@Bi	Mn_{6c}	527	550(30)	$-B_3$
● Te-μ-Bi@Mn	Bi_{3a}	95	0(80)	$-\Delta B_1$

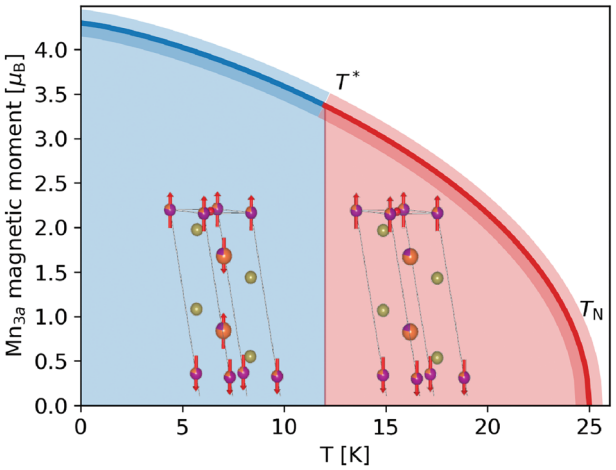

Figure 4. $MnBi_2Te_4$ phase diagram summary: temperature dependence of the Mn_{3a} magnetic moment, rescaled from the μSR fields $\Delta B_1(T)$, $B_2(T)$, and $T \to 0$ value obtained from ZF Mn_{3a} NMR (shaded bands translate uncertainty in the latter). Insets: magnetic structures in one septuple layer of the primitive cell.

scattering, to distinguish the reduction of the magnetic moment, encoded in the local field, from the volume fraction, encoded in the amplitude of the signal. Local disorder, like that expected from magnetically coupled, random antisites, could yield a distribution of transition temperatures, and hence a more progressive reduction of the volume fraction than that displayed in all our samples. This suggests that, from a magnetic point of view, the high-temperature ordered phase approaches closely the ideal, intermixing-free material. This provides both the antiferromagnetic and the ferromagnetic versions of a close-to-ideal magnetic topological insulator. This discovery is highly relevant in the context of the crucial role that Mn-Bi intermixing plays in the reduction of the gap at the Dirac point in $MnBi_2Te_4$.[41–44,56–61] Indeed, a recent scanning tunneling spectroscopy study reveals that the surface gap is absent in the regions with a high degree of intermixing, while the areas with the lower degree of intermixing show gapped spectra.[42] According to density functional theory calculations[41] the antiferromagnetic coupling between the Mn_{3a} and Mn_{6c} sublattices is responsible for the gap reduction or suppression. Photoemission data[41,61] also show a gap reduction due to the presence of antisites; unfortunately they do not elucidate the gap behavior across T^*, which remains an open question for further experiments.

Early sublattice decoupling is well documented, for instance in intermetallic compounds,[78–85] and it often involves exchange coupling frustration, which may also play a role in the present case.[86] Since intermixing is a common feature for all materials, including cation species with similar radii, we speculate that early antisite disordering may take place more often than one thinks. Therefore, our findings may have a more general impact than just on the present materials.

5. Experimental Section

Synthesis: Polycrystalline samples of $(MnBi_2Te_4)(Bi_2Te_3)_n$ with n = 0, 1, 2 and of $MnSb_2Te_4$ were prepared by high-temperature solid-state reactions following in general the protocols described in the previous works.[30,45,48,63] The polycrystals were kept as non-compacted powders for NMR experiments, and pressed into pellets for the μSR experiments. Single crystal experiments were also performed with both techniques with very similar results, although with much smaller signal to noise ratio, and the extensive studies were restricted to the polycrystalline samples.

Two $MnBi_2Te_4$ (denoted α and β) powdered samples were obtained by two distinct high-temperature annealing routes. The $MnBi_2Te_4$ α-sample was prepared from a mixture of pre-synthesized MnTe and Bi_2Te_3 taken in the ratio 0.87:1.05. The powders were handled in an argon-filled dry glovebox (MBraun), homogenized in a dry ball-mill (Retsch, MM400) at 20 Hz for 20 min and then pressed into a 6-mm pellet (2 tons, 30 s). The pressling was placed into a quartz ampoule, sealed off under dynamic vacuum (3×10^{-3} mbar) and annealed in a temperature-controlled tube furnace (Reetz GmbH) following the procedure developed in ref. [63].

The polycrystalline $MnBi_2Te_4$ β-sample was synthesized by co-melting of pre-synthesized MnTe and Bi_2Te_3 in an evacuated quartz ampoule at a temperature of about 980 °C for 12 h, followed by slow cooling down to 580 °C at the rate of 5° h^{-1}. This temperature was kept for 12 h followed by air-quenching. Then, the polycrystalline sample was ground as a fine powder and converted into a pellet and was then sealed in a quartz container under the pressure of 10^{-4} Pa. The ampoule was further heated up to 585 °C for 8 h, then kept at this temperature for about 240 h followed by air-quenching. The grinding and annealing process was repeated twice to achieve a homogenized phase-pure compound.

The $MnBi_4Te_7$ and $MnBi_6Te_{10}$ samples were obtained from a corresponding, stoichiometric mixture of the powdered binaries that were handled similar to the ones above. The former was annealed at 585 °C for 10 days (heating rate 1° h^{-1}) and the latter was annealed at 575 °C for 4 days (heating rate 90° h^{-1}). Both samples were water-quenched.

The $MnSb_2Te_4$ sample was synthesized from a stoichiometric mixture of the elements (Sigma–Aldrich, 9N5, Mn reduced prior to synthesis) that was ball-milled at 20 Hz for 20 min, pelletized and annealed at 550 °C for 8 days, and finally quenched.

X-Ray Diffraction and Energy-Dispersive X-Ray Spectroscopy: Phase purity of all samples but β was analyzed by powder X-ray diffraction (PXRD) on a Malvern Panalytical Empyrean three diffractometer, employing $CuK\alpha_1$ radiation (λ = 1.54059 Å) and set in Bragg-Brentano geometry. Lattice parameters refinement was conducted by Le Bail method to ensure the correct assignment of the $(MnBi_2Te_4)(Bi_2Te_3)_n$ phases. A PXRD pattern of the β-sample was taken on a Bruker D2 PHASER diffractometer using $CuK\alpha_1$ radiation within the scanning range of $2\theta = 5 - 75$. The details of phase analysis for all $(MnBi_2Te_4)(Bi_2Te_3)_n$,samples are given in the Supporting Information (Figures S1–S6, Supporting Information); the obtained results were in line with the previously published results.[28–30,45,63]

$MnSb_2Te_4$ accommodates strong Mn/Sb intermixing[47,48,87] and, therefore, adopt various total compositions. To achieve the highest accuracy in the determination of the chemical composition of the powdered sample, calibrated EDX measurements were conducted. For that, parts of the sample were cast into synthetic resin (versosit) pucks, sputtered with a gold layer and painted with conductive silver paint to avoid charge accumulation. EDX spectra were recorded with a high-resolution SEM EVOMA 15 (Zeiss) equipped with a Peltier-cooled Si(Li) detector (Oxford Instruments) employing 30 kV acceleration voltage. Element quantification was obtained from least-square fitting of edge models (Mn-K, Te-L, Sb-L) invoking k-factor calibration from the stoichiometric samples of similar composition (Sb_2Te_3 and MnTe). To assess systematic errors stemming from the different edge and reference choices, Sb_2Te_3 and MnTe references are included for Te in the quantification statistics. The determined composition of the sample was $Mn_{0.87(1)}Sb_{2.03(1)}Te_{4.00(1)}$, which was in line with its magnetic properties reported in Ref. [69].

NMR: The NMR spectra were measured in a He-flow cryostat by means of the HyReSpect home-built phase coherent broadband spectrometer.[88] Spin-echoes were excited at discrete frequency points by refocusing P–τ–P Hahn radio-frequency (rf) pulse sequences, with optimized pulse duration and intensity to maximize the resonance signal, and shortest τ delay (limited by the apparatus dead time of few μs).

Spectra were reconstructed from the maximum of the spin-echo Fourier transform amplitude at each frequency, corrected for the frequency-dependent sensitivity and nuclear Boltzmann factors. The normalized values correspond to the spectral distribution of hyperfine fields at the ^{55}Mn nuclei. When the best fit of the two spectra ($\zeta = Mn_{3a}$, Mn_{6c}) require more than one Gaussian component each, their mean frequency was calculated from the corresponding weights $A_{\alpha,\,i}$ as the first moment $\sum_i A_{\zeta i} \nu_{\zeta i} / \sum_k A_{\zeta,k}$.

ZF nuclear echoes were collected with a non-resonant probe circuit, by virtue of the large rf enhancement $\eta = H_1^*/H_1$, where H_1 was the applied field at the radio frequency ω, and H_1^* is the ω oscillating component of the huge hyperfine field B_{hf}, following the electronic moment response to H_1.[89,90] The factor η was very sensitive to nanoscopic and mesoscopic changes in the nucleus environment and this did not guarantee a uniform proportionality between spectral area and number of resonating nuclei. Relative proportionality was recovered in the more uniform resonant conditions obtained at high static applied fields.

μSR: The μSR experiments were carried out at the Paul Scherrer Institute, Villigen, Switzerland, on the GPS spectrometer.

A minimal choice for the best-fit function of the time domain ZF asymmetry, arising from parity violation in the weak muon decay, was the following

$$A_{ZF}(t) = A_0 \left[f_{T1}\, e^{-\sigma_1^2 t^2/2} + \sum_{i=2}^{3} f_{Ti}\, \cos(\gamma_\mu B_1 t)\, e^{-\sigma_i^2 t^2/2} + f_L\, e^{-t/T_1} \right] \quad (2)$$

distinguishing the fast relaxing, precessing fractions $f_T = \sum_{i=1}^{3} f_{Ti}$ (T for transverse with respect to the initial muon spin direction) from the slow relaxing fraction f_L (L for longitudinal), which corresponds to local field components parallel to the initial muon spin direction. The precession relaxation rates were due to the width of each field distribution, $\sigma_i = 2\pi\gamma_\mu \Delta B_i$, their fractions obey $f_T + f_L = 1$ and the maximum experimental asymmetry, A_0, is calibrated at high temperature. Polycrystalline averaging leads to $2f_L = f_T$, but a very fast transverse decay and a small fraction of muons stopping outside the sample may relax this ideal condition.

The WFT time domain signals were best fitted by an oscillatory and two relaxing functions

$$A_{TF}(t) = A_0 \left[f_p\, \cos(\gamma B + \phi)\, e^{-\lambda_p t} + f_T\, e^{\sigma_T^2 t^2/2} + f_L\, e^{-\lambda_L t} \right] \quad (3)$$

where ϕ is an initial phase and f_p is the muon fraction that does not experience strong local hyperfine fields, which includes muons stopping outside the sample and inside paramagnetic microdomains. The former corresponds to the low temperature residual value f_{p0}, whereas for $T \ll T_m$, one has $f_p = 1$, $f_T = f_L = 0$. The two relaxing function represent the transverse and longitudinal fractions of muons experiencing internal fields.

Three independent determinations of the magnetic volume fraction were given by

$$m_{wtf}(t) = \frac{f_p(T) - f_{p0}}{1 - f_{p0}} \quad (4)$$

$$m_T = \sum_{i=1}^{3} m_i \qquad m_i = \frac{f_{Ti}}{f_{t0}} \quad (5)$$

$$m_L = = \frac{3}{2}(1 - f_L(T)) \quad (6)$$

where $f_{T0} = \lim_{T \to 0} f_T(T)$ and Equation (5) neglects f_{p0}, since in ZF f_L is indistinguishable from f_p. They are used in Figure 2g,h (Equation (4)) and j (Equation (5) colored and gray symbols, for Equations (5) and (6), respectively).

Lastly, the internal fields $\Delta B_1 = \sigma_1/2\pi\gamma_\mu$, and B_2 proportional to the order parameter are fitted to a standard phenomenological function[91]

$$b(T) = \left[1 - \left(\frac{T}{T_m} \right)^{\gamma} \right]^{\delta} \quad (7)$$

used both in the shaded colors of Figure 2d–f and in Figures 4 and Figure S8 (Supporting Information).

DFT: The DFT calculation protocols for determining the muon implantation sites[70] and the contact contribution to the hyperfine interactions in magnetic compounds[71,72] were well established. State of the art DFT calculations were performed on a magnetic supercell, including an extra impurity hydrogen atom. Sampling of the starting impurity supercell coordinates and lattice relaxation by force minimization yield minimum total energy sites and their spin couplings, that allow the calculation of the local field.[73] Full calculation details are reported in the Supporting Information.[62]

Supporting Information

Supporting Information is available from the Wiley Online Library or from the author.

Acknowledgements

M.S. and I.J.O. contributed equally to this work. This work was supported by the Deutsche Forschungsgemeinschaft (DFG) within the Würzburg-Dresden Cluster of Excellence on Complexity and Topology in Quantum Matter – *ct.qmat* (EXC 2147, project-id 390858490) and the SFB 1143 (project-id 247310070). I.J.O. and R.D.R. acknowledged financInformationial support from PNRR MUR project ECS-00000033-ECOSISTER and also acknowledged computing resources provided by the STFC scientific computing department's SCARF cluster and CINECA under ISCRA Project ID IsCa4. Z.S. acknowledged support by the Swiss National Science Foundation (SNF-Grant No. 200021_165910). L.T.C. was funded by the DFG (project-id 456950766). The cost of the HyReSpect equipment used for this investigation was partly supported by the University of Parma through the Scientific Instrumentation Upgrade Program 2020. This work was partially based on experiments performed at the Swiss MuonInformation Source (SμS), Paul Scherrer Institute, Villigen, Switzerland. M.M.O. acknowledged the support by MCIN/ AEI /10.13039/ 501100011033/ (Grant PID2022-138210NB-I00) and "ERDF A way of making Europe", MCIN with funding from European Union NextGenerationEU (PRTR-C17.I1) promoted by the Government of Aragon as well as Ayuda CEX2023-001286-S financiada por MICIU/AEI/10.13039/501100011033. E.V.C. acknowledges Saint-Petersburg State University for a research project 95442847. The authors acknowledged Dr. Alexander Zeugner, MSc. Fabian Lukas and MSc. Laura Mengs (Technische Universität Dresden) for their contributions to sample preparations. The authors are grateful to the group of Prof. A. Lubk (TU Dresden, IFW Dresden) and to Mrs. G. Kreutzer for the calibrated EDX measurements and insightful discussions.

Conflict of Interest

The authors declare no conflict of interest.

Data Availability Statement

The original data are available at http://musruser.psi.ch, instrument GPS, years 2020, 2021, title includes the chemical formula. NMR data, the DFT input and results are available at Materials Cloud Archive https://archive.materialscloud.org/record/2024.20 DOI:10.24435/materialscloud:he-f5.

Keywords

cation intermixing, magnetic topological insulators, magnetic transitions

Received: March 15, 2024
Revised: May 22, 2024
Published online: July 8, 2024

[1] X.-L. Qi, S.-C. Zhang, *Rev. Mod. Phys.* **2011**, *83*, 1057.
[2] Y. Tokura, K. Yasuda, A. Tsukazaki, *Nat. Rev. Phys.* **2019**, *1*, 126.
[3] P. Wang, J. Ge, J. Li, Y. Liu, Y. Xu, J. Wang, *The Innovation* **2021**, *2*, 100098.
[4] B. A. Bernevig, C. Felser, H. Beidenkopf, *Nature* **2022**, *603*, 41.
[5] C.-Z. Chang, C.-X. Liu, A. H. MacDonald, *Rev. Mod. Phys.* **2023**, *95*, 011002.
[6] C.-Z. Chang, J. Zhang, X. Feng, J. Shen, Z. Zhang, M. Guo, K. Li, Y. Ou, P. Wei, L.-L. Wang, Z.-Q. Ji, Y. Feng, S. Ji, X. Chen, J. Jia, X. Dai, Z. Fang, S.-C. Zhang, K. He, Y. Wang, L. Lu, X.-C. Ma, Q.-K. Xue, *Science* **2013**, *340*, 167.
[7] J. Checkelsky, R. Yoshimi, A. Tsukazaki, K. Takahashi, Y. Kozuka, J. Falson, M. Kawasaki, Y. Tokura, *Nat. Phys.* **2014**, *10*, 731.
[8] D. M. Nenno, C. A. Garcia, J. Gooth, C. Felser, P. Narang, *Nat. Rev. Phys.* **2020**, *2*, 682.
[9] A. Sekine, K. Nomura, *J. Appl. Phys.* **2021**, *129*, 14.
[10] J.-X. Qiu, C. Tzschaschel, J. Ahn, A. Gao, H. Li, X.-Y. Zhang, B. Ghosh, C. Hu, Y.-X. Wang, Y.-F. Liu, D. Bérubé, T. Dinh, Z. Gong, S.-W. Lien, S.-C. Ho, B. Singh, K. Watanabe, T. Taniguchi, D. C. Bell, H.-Z. Lu, A. Bansil, H. Lin, T.-R. Chang, B. B. Zhou, Q. Ma, A. Vishwanath, N. Ni, S.-Y. Xu, *Nat. Mater.* **2023**, *22*, 583.
[11] M. M. Otrokov, I. I. Klimovskikh, H. Bentmann, D. Estyunin, A. Zeugner, Z. S. Aliev, S. Gaß, A. Wolter, A. Koroleva, A. M. Shikin, M. Blanco-Rey, M. Hoffmann, I. P. Rusinov, A. Y. Vyazovskaya, S. V. Eremeev, Yu. M. Koroteev, V. M. Kuznetsov, F. Freyse, J. Sánchez-Barriga, I. R. Amiraslanov, M. B. Babanly, N. T. Mamedov, N. A. Abdullayev, V. N. Zverev, A. Alfonsov, V. Kataev, B. Büchner, E. F. Schwier, S. Kumar, A. Kimura, et al., *Nature* **2019**, *576*, 416.
[12] J. Li, Y. Li, S. Du, Z. Wang, B.-L. Gu, S.-C. Zhang, K. He, W. Duan, Y. Xu, *Sci. Adv.* **2019**, *5*, eaaw5685.
[13] D. Zhang, M. Shi, T. Zhu, D. Xing, H. Zhang, J. Wang, *Phys. Rev. Lett.* **2019**, *122*, 206401.
[14] Y. Gong, J. Guo, J. Li, K. Zhu, M. Liao, X. Liu, Q. Zhang, L. Gu, L. Tang, X. Feng, D. Zhang, W. Li, C. Song, L. Wang, P. Yu, X. Chen, Y. Wang, H. Yao, W. Duan, Y. Xu, S.-C. Zhang, X. Ma, Q.-K. Xue, K. He, *Chin. Phys. Lett.* **2019**, *36*, 076801.
[15] J.-Q. Yan, Q. Zhang, T. Heitmann, Z. Huang, K. Y. Chen, J.-G. Cheng, W. Wu, D. Vaknin, B. C. Sales, R. J. McQueeney, *Phys. Rev. Mater.* **2019**, *3*, 064202.
[16] R. S. K. Mong, A. M. Essin, J. E. Moore, *Phys. Rev. B* **2010**, *81*, 245209.
[17] M. M. Otrokov, I. P. Rusinov, M. Blanco-Rey, M. Hoffmann, A. Y. Vyazovskaya, S. V. Eremeev, A. Ernst, P. M. Echenique, A. Arnau, E. V. Chulkov, *Phys. Rev. Lett.* **2019**, *122*, 107202.
[18] J. Li, Y. Li, S. Du, Z. Wang, B.-L. Gu, S.-C. Zhang, K. He, W. Duan, Y. Xu, *Sci. Adv.* **2019**, *5*, eaaw5685.
[19] C. Liu, Y. Wang, H. Li, Y. Wu, Y. Li, J. Li, K. He, Y. Xu, J. Zhang, Y. Wang, *Nat. Mater.* **2020**, *19*, 522.
[20] A. Gao, Y.-F. Liu, C. Hu, J.-X. Qiu, C. Tzschaschel, B. Ghosh, S.-C. Ho, D. Bérubé, R. Chen, H. Sun, Z. Zhang, X.-Y. Zhang, Y.-X. Wang, N. Wang, Z. Huang, C. Felser, A. Agarwal, T. Ding, H.-J. Tien, A. Akey, J. Gardener, B. Singh, K. Watanabe, T. Taniguchi, K. S. Burch, D. C. Bell, B. B. Zhou, W. Gao, H.-Z. Lu, A. Bansil, et al., *Nature* **2021**, *595*, 521.
[21] J. Ge, Y. Liu, J. Li, H. Li, T. Luo, Y. Wu, Y. Xu, J. Wang, *National Science Review* **2020**, *7*, 1280.
[22] Y. Deng, Y. Yu, M. Z. Shi, Z. Guo, Z. Xu, J. Wang, X. H. Chen, Y. Zhang, *Science* **2020**, *367*, 895.
[23] J.-Q. Yan, S. Okamoto, M. A. McGuire, A. F. May, R. J. McQueeney, B. C. Sales, *Phys. Rev. B* **2019**, *100*, 104409.
[24] S. Wimmer, J. Sánchez-Barriga, P. Küppers, A. Ney, E. Schierle, F. Freyse, O. Caha, J. Michalička, M. Liebmann, D. Primetzhofer, M. Hoffman, A. Ernst, M. M. Otrokov, G. Bihlmayer, E. Weschke, B. Lake, E. V. Chulkov, M. Morgenstern, G. Bauer, G. Springholz, O. Rader, *Adv. Mater.* **2021**, *33*, 2102935.
[25] S. H. Lee, D. Graf, L. Min, Y. Zhu, H. Yi, S. Ciocys, Y. Wang, E. S. Choi, R. Basnet, A. Fereidouni, A. Wegner, Y.-F. Zhao, K. Verlinde, J. He, R. Redwing, V. Gopalan, H. O. H. Churchill, A. Lanzara, N. Samarth, C.-Z. Chang, J. Hu, Z. Q. Mao, *Phys. Rev. X* **2021**, *11*, 031032.
[26] T. Zhu, A. J. Bishop, T. Zhou, M. Zhu, D. J. O'Hara, A. A. Baker, S. Cheng, R. C. Walko, J. J. Repicky, T. Liu, J. A. Gupta, C. M. Jozwiak, E. Rotenberg, J. Hwang, I. Žutic, R. K. Kawakami, *Nano Lett.* **2021**, *21*, 5083.
[27] L. Cao, S. Han, Y.-Y. Lv, D. Wang, Y.-C. Luo, Y.-Y. Zhang, S.-H. Yao, J. Zhou, Y. B. Chen, H. Zhang, Y.-F. Chen, *Phys. Rev. B* **2021**, *104*, 054421.
[28] Z. S. Aliev, I. R. Amiraslanov, D. I. Nasonova, A. V. Shevelkov, N. A. Abdullayev, Z. A. Jahangirli, E. N. Orujlu, M. M. Otrokov, N. T. Mamedov, M. B. Babanly, E. V. Chulkov, *J. Alloys Compd.* **2019**, *789*, 443.
[29] D. Souchay, M. Nentwig, D. Günther, S. Keilholz, J. de Boor, A. Zeugner, A. Isaeva, M. Ruck, A. U. Wolter, B. Büchner, O. Oeckler, *J. Mater. Chem. C* **2019**, *7*, 9939.
[30] R. Vidal, A. Zeugner, J. Facio, R. Ray, M. Haghighi, A. Wolter, L. CorredorBohorquez, F. Caglieris, S. Moser, T. Figgemeier, T. Peixoto, H. Vasili, M. Valvidares, S. Jung, C. Cacho, A. Alfonsov, K. Mehlawat, V. Kataev, C. Hess, M. Richter, B. Buchner, J. vandenBrink, M. Ruck, F. Reinert, H. Bentmann, A. Isaeva, *Phys. Rev. X* **2019**, *9*, 041065.
[31] J. Wu, F. Liu, M. Sasase, K. Ienaga, Y. Obata, R. Yukawa, K. Horiba, H. Kumigashira, S. Okuma, T. Inoshita, H. Hosono, *Sci. Adv.* **2019**, *5*, eaax9989.
[32] M. Z. Shi, B. Lei, C. S. Zhu, D. H. Ma, J. H. Cui, Z. L. Sun, J. J. Ying, X. H. Chen, *Phys. Rev. B* **2019**, *100*, 155144.
[33] C. Hu, K. N. Gordon, P. Liu, J. Liu, X. Zhou, P. Hao, D. Narayan, E. Emmanouilidou, H. Sun, Y. Liu, H. Brawer, A. P. Ramirez, L. Ding, H. Cao, Q. Liu, D. Dessau, N. Ni, *Nat. Commun.* **2020**, *11*, 97.
[34] I. I. Klimovskikh, M. M. Otrokov, D. Estyunin, S. V. Eremeev, S. O. Filnov, A. Koroleva, E. Shevchenko, V. Voroshnin, A. G. Rybkin, I. P. Rusinov, M. Blanco-Rey, M. Hoffmann, Z. S. Aliev, M. B. Babanly, I. R. Amiraslanov, N. A. Abdullayev, V. N. Zverev, A. Kimura, O. E. Tereshchenko, K. A. Kokh, L. Petaccia, G. D. Santo, A. Ernst, P. M. Echenique, N. T. Mamedov, A. M. Shikin, E. V. Chulkov, *npj Quantum Mater.* **2020**, *5*, 54.
[35] J. Shao, Y. Liu, M. Zeng, J. Li, X. Wu, X.-M. Ma, F. Jin, R. Lu, Y. Sun, M. Gu, K. Wang, W. Wu, L. Wu, C. Liu, Q. Liu, Y. Zhao, *Nano Lett.* **2021**, *21*, 5874.
[36] R.-X. Zhang, F. Wu, S. Das Sarma, *Phys. Rev. Lett.* **2020**, *124*, 136407.
[37] C. Hu, L. Ding, K. N. Gordon, B. Ghosh, H.-J. Tien, H. Li, A. G. Linn, S.-W. Lien, C.-Y. Huang, S. Mackey, J. Liu, P. V. S. Reddy, B. Singh, A. Agarwal, A. Bansil, M. Song, D. Li, S.-Y. Xu, H. Lin, H. Cao, T.-R. Chang, D. Dessau, N. Ni, *Sci. Adv.* **2020**, *6*, eaba4275.
[38] A. Tan, V. Labracherie, N. Kunchur, A. Wolter, J. Cornejo, J. Dufouleur, B. Buchner, A. Isaeva, R. Giraud, *Phys. Rev. Lett.* **2020**, *124*, 197201.
[39] Y. Liu, L.-L. Wang, Q. Zheng, Z. Huang, X. Wang, M. Chi, Y. Wu, B. C. Chakoumakos, M. A. McGuire, B. C. Sales, W. Wu, J. Yan, *Phys. Rev. X* **2021**, *11*, 021033.
[40] Y. Lai, L. Ke, J. Yan, R. D. McDonald, R. J. McQueeney, *Phys. Rev. B* **2021**, *103*, 184429.
[41] M. Garnica, M. Otrokov, P. C. Aguilar, I. Klimovskikh, D. Estyunin, Z. Aliev, I. Amiraslanov, N. Abdullayev, V. Zverev, M. Babanly, N. T. Mamedov, A. M. Shikin, A. Arnau, A. L. V. de Parga, E. V. Chulkov, R. Miranda, *npj Quantum Mater.* **2022**, *7*, 7.
[42] M. Liu, C. Lei, H. Kim, Y. Li, L. Frammolino, J. Yan, A. H. Macdonald, C.-K. Shih, *Proc. Natl. Acad. Sci. U.S.A.* **2022**, *119*, e2207681119.
[43] H. Tan, B. Yan, *Phys. Rev. Lett.* **2023**, *130*, 126702.

[44] F. Lüpke, M. Kolmer, J. Yan, H. Chang, P. Vilmercati, H. H. Weitering, W. Ko, A.-P. Li, *Communications Materials* **2023**, *4*, 82.
[45] A.-V. Tcakaev, B. Rubrecht, J. I. Facio, V. B. Zabolotnyy, L. T. Corredor, L. C. Folkers, E. Kochetkova, T. R. Peixoto, P. Kagerer, S. Heinze, H. Bentmann, R. J. Green, P. Gargiani, M. Valvidares, E. Weschke, M. W. Haverkort, F. Reinert, J. van den Brink, B. Büchner, A. U. B. Wolter, A. Isaeva, V. Hinkov, *Adv. Sci.* **2023**, *10*, 2203239.
[46] C. Yan, Y. Zhu, L. Miao, S. Fernandez-Mulligan, E. Green, R. Mei, H. Tan, B. Yan, C.-X. Liu, N. Alem, Z. Mao, S. Yang, *Nano Lett.* **2022**, *22*, 9815.
[47] M. Sahoo, M. Rahn, E. Kochetkova, O. Renier, L. Folkers, A. Tcakaev, M. Amigó, F. Stier, V. Pomjakushin, K. Srowik, V. Zabolotnyy, E. Weschke, V. Hinkov, A. Alfonsov, V. Kataev, B. Büchner, A. Wolter, J. Facio, L. Corredor, A. Isaeva, *Materials Today Physics* **2023**, *38*, 101265.
[48] L. C. Folkers, L. T. Corredor, F. Lukas, M. Sahoo, A. U. Wolter, A. Isaeva, *Z. Kristallogr. Cryst. Mater.* **2022**, *237*, 101.
[49] M.-H. Du, J. Yan, V. R. Cooper, M. Eisenbach, *Adv. Funct. Mater.* **2021**, *31*, 2006516.
[50] T. Murakami, Y. Nambu, T. Koretsune, G. Xiangyu, T. Yamamoto, C. M. Brown, H. Kageyama, *Phys. Rev. B* **2019**, *100*, 195103.
[51] S. K. Chong, C. Lei, J. Li, Y. Cheng, D. Graf, S. H. Lee, M. Tanabe, T.-H. Yang, Z. Mao, A. H. MacDonald, K. L. Wang, *arXiv preprint arXiv:2306.10325* **2023**.
[52] S. X. M. Riberolles, Q. Zhang, E. Gordon, N. P. Butch, L. Ke, J.-Q. Yan, R. J. McQueeney, *Phys. Rev. B* **2021**, *104*, 064401.
[53] J.-Q. Yan, Y. H. Liu, D. S. Parker, Y. Wu, A. A. Aczel, M. Matsuda, M. A. McGuire, B. C. Sales, *Phys. Rev. Materials* **2020**, *4*, 054202.
[54] L. Ding, C. Hu, F. Ye, E. Feng, N. Ni, H. Cao, *Phys. Rev. B* **2020**, *101*, 020412.
[55] L. Ding, C. Hu, E. Feng, C. Jiang, I. A. Kibalin, A. Gukasov, M. Chi, N. Ni, H. Cao, *J. Phys. D: Appl. Phys.* **2021**, *54*, 174003.
[56] Y.-J. Hao, P. Liu, Y. Feng, X.-M. Ma, E. F. Schwier, M. Arita, S. Kumar, C. Hu, R. Lu, M. Zeng, Y. Wang, Z. Hao, H.-Y. Sun, K. Zhang, J. Mei, N. Ni, L. Wu, K. Shimada, C. Chen, Q. Liu, C. Liu, *Phys. Rev. X* **2019**, *9*, 041038.
[57] H. Li, S.-Y. Gao, S.-F. Duan, Y.-F. Xu, K.-J. Zhu, S.-J. Tian, J.-C. Gao, W.-H. Fan, Z.-C. Rao, J.-R. Huang, J.-J. Li, D.-Y. Yan, Z.-T. Liu, W.-L. Liu, Y.-B. Huang, Y.-L. Li, Y. Liu, G.-B. Zhang, P. Zhang, T. Kondo, S. Shin, H.-C. Lei, Y.-G. Shi, W.-T. Zhang, H.-M. Weng, T. Qian, H. Ding, *Phys. Rev. X* **2019**, *9*, 041039.
[58] Y. J. Chen, L. X. Xu, J. H. Li, Y. W. Li, H. Y. Wang, C. F. Zhang, H. Li, Y. Wu, A. J. Liang, C. Chen, S. W. Jung, C. Cacho, Y. H. Mao, S. Liu, M. X. Wang, Y. F. Guo, Y. Xu, Z. K. Liu, L. X. Yang, Y. L. Chen, *Phys. Rev. X* **2019**, *9*, 041040.
[59] P. Swatek, Y. Wu, L.-L. Wang, K. Lee, B. Schrunk, J. Yan, A. Kaminski, *Phys. Rev. B* **2020**, *101*, 161109(R).
[60] D. Nevola, H. X. Li, J.-Q. Yan, R. G. Moore, H.-N. Lee, H. Miao, P. D. Johnson, *Phys. Rev. Lett.* **2020**, *125*, 117205.
[61] A. M. Shikin, D. A. Estyunin, N. L. Zaitsev, D. Glazkova, I. I. Klimovskikh, S. O. Filnov, A. G. Rybkin, E. F. Schwier, S. Kumar, A. Kimura, N. Mamedov, Z. Aliev, M. B. Babanly, K. Kokh, O. E. Tereshchenko, M. M. Otrokov, E. V. Chulkov, K. A. Zvezdin, A. K. Zvezdin, *Phys. Rev. B* **2021**, *104*, 115168.
[62] Supplemental Material.
[63] A. Zeugner, F. Nietschke, A. U. Wolter, S. Gaß, R. C. Vidal, T. R. Peixoto, D. Pohl, C. Damm, A. Lubk, R. Hentrich, S. K. Moser, C. Fornari, C. H. Min, S. Schatz, K. Kißner, M. Ünzelmann, M. Kaiser, F. Scaravaggi, B. Rellinghaus, K. Nielsch, C. Hess, B. Büchner, F. Reinert, H. Bentmann, O. Oeckler, T. Doert, M. Ruck, A. Isaeva, *Chem. Mater.* **2019**, *31*, 2795.
[64] S. H. Lee, Y. Zhu, Y. Wang, L. Miao, T. Pillsbury, H. Yi, S. Kempinger, J. Hu, C. A. Heikes, P. Quarterman, W. Ratcliff, J. A. Borchers, H. Zhang, X. Ke, D. Graf, N. Alem, C.-Z. Chang, N. Samarth, Z. Mao, *Phys. Rev. Res.* **2019**, *1*, 012011.
[65] S.-K. Bac, K. Koller, F. Lux, J. Wang, L. Riney, K. Borisiak, W. Powers, M. Zhukovskyi, T. Orlova, M. Dobrowolska, J. K. Furdyna, N. R. Dilley, L. P. Rokhinson, Y. Mokrousov, R. J. McQueeney, O. Heinonen, X. Liu, B. A. Assaf, *npj Quantum Mater.* **2022**, *7*, 46.
[66] P. M. Sass, W. Ge, J. Yan, D. Obeysekera, J. Yang, W. Wu, *Nano Lett.* **2020**, *20*, 2609.
[67] I. R. Amiraslanov, Z. S. Aliev, P. A. Askerova, E. H. Alizade, Y. N. Aliyeva, N. A. Abdullayev, Z. A. Jahangirli, M. M. Otrokov, N. T. Mamedov, E. V. Chulkov, *Phys. Rev. B* **2022**, *106*, 184108.
[68] R. Lu, H. Sun, S. Kumar, Y. Wang, M. Gu, M. Zeng, Y.-J. Hao, J. Li, J. Shao, X.-M. Ma, Z. Hao, K. Zhang, W. Mansuer, J. Mei, Y. Zhao, C. Liu, K. Deng, W. Huang, B. Shen, K. Shimada, E. F. Schwier, C. Liu, Q. Liu, C. Chen, *Phys. Rev. X* **2021**, *11*, 011039.
[69] M. Sahoo, Z. Salman, G. Allodi, A. Isaeva, L. Folkers, A. Wolter, B. Büchner, R. De Renzi, in *Journal of Physics: Conference Series*, vol. *2462*. IOP Publishing, Bristol, England **2023**, pp. 012040.
[70] J. S. Möller, P. Bonfà, D. Ceresoli, F. Bernardini, S. J. Blundell, T. Lancaster, R. D. Renzi, N. Marzari, I. Watanabe, S. Sulaiman, M. I. Mohamed-Ibrahim, *Phys. Scr.* **2013**, *88*, 068510.
[71] P. Bonfà, R. De Renzi, *J. Phys. Soc. Jpn.* **2016**, *85*, 091014.
[72] I. J. Onuorah, P. Bonfà, R. De Renzi, *Phys. Rev. B* **2018**, *97*, 174414.
[73] P. Bonfà, I. J. Onuorah, R. D. Renzi, *Introduction and a Quick Look at MUESR, the Magnetic Structure and mUon Embedding Site Refinement Suite*, the Physical Society of Japan, Yushima **2018**.
[74] A. Freeman, R. Watson, *Magnetism IIA*, Academic Press, Cambridge **1965**.
[75] J. Freeman, R. E. Watson, in *Treatise on Magnetism IIA* (Eds: G. Rado, H. SaM), Academic Press, Inc., New York **1965**, p. 167.
[76] G. Allodi, M. Cestelli Guidi, R. De Renzi, M. Pieper, *J. Magn. Magn. Mater.* **2002**, *242–245*, 635.
[77] L. Ding, C. Hu, F. Ye, E. Feng, N. Ni, H. Cao, *Phys. Rev. B* **2020**, *101*, 020412(R).
[78] F. Cugini, S. Chicco, F. Orlandi, G. Allodi, P. Bonfá, V. Vezzoni, O. N. Miroshkina, M. E. Gruner, L. Righi, S. Fabbrici, F. Albertini, R. De Renzi, M. Solzi, *Phys. Rev. B* **2022**, *105*, 174434.
[79] A. Wills, *J. Phys. IV France* **2001**, *11*, Pr9.
[80] F. Damay, J. Sottmann, F. Lainé, L. Chaix, M. Poienar, P. Beran, E. Elkaim, F. Fauth, L. Nataf, A. Guesdon, A. Maignan, C. Martin, *Phys. Rev. B* **2020**, *101*, 094418.
[81] V. O. Garlea, L. D. Sanjeewa, M. A. McGuire, C. D. Batista, A. M. Samarakoon, D. Graf, B. Winn, F. Ye, C. Hoffmann, J. W. Kolis, *Phys. Rev. X* **2019**, *9*, 011038.
[82] J. Cadogan, D. Ryan, *J. Alloys Compd.* **2001**, *326*, 166.
[83] R. Morrow, R. Mishra, O. D. Restrepo, M. R. Ball, W. Windl, S. Wurmehl, U. Stockert, B. Büchner, P. M. Woodward, *J. Am. Chem. Soc.* **2013**, *135*, 18824.
[84] I. Lyubutin, V. Terziev, S. Luchko, A. Shapiro, A. Balagurov, G. Bonch-Osmolovskiy, *Physica C: Superconductivity* **1992**, *199*, 296.
[85] F. Orlandi, S. Fabbrici, F. Albertini, P. Manuel, D. D. Khalyavin, L. Righi, *Phys. Rev. B* **2016**, *94*, 140409(R).
[86] H. Li, Y. Li, Y. Lian, W. Xie, L. Chen, J. Zhang, Y. Wu, S. Fan, *Sci. China Mater.* **2022**, *65*, 477.
[87] Y. Liu, L.-L. Wang, Q. Zheng, Z. Huang, X. Wang, M. Chi, Y. Wu, B. C. Chakoumakos, M. A. McGuire, B. C. Sales, W. Wu, J. Yan, *Phys. Rev. X* **2021**, *11*, 021033.
[88] G. Allodi, A. Banderini, R. De Renzi, C. Vignali, *Rev. Sci. Instrum.* **2005**, *76*, 083911.
[89] C. Meny, P. Panissod, *Annual Reports on NMR Spectroscopy*, vol. *103*, Academic Press, Cambridge **2021**, pp. 47–96.
[90] A. A. Sidorenko, G. Allodi, R. De Renzi, G. Balestrino, M. Angeloni, *Phys. Rev. B* **2006**, *73*, 054406.
[91] S. J. Blundell, R. De Renzi, T. Lancaster, F. L. e. Pratt, *Introduction to Muon Spectroscopy*, Oxford University Press, Oxford **2022**.